Research Square

Preprints are preliminary reports that have not undergone peer review.
They should not be considered conclusive, used to inform clinical practice,
or referenced by the media as validated information.

# Hybrid Analytical–Ann Modelling of Free Vibration in Porous Functionally Graded Nanobeams

**abdelhakim Bouhadra**

abdelhakim.bouhadra@univ-khenchela.dz

University of Khenchela

**Djamel Eddine Lafi**

Ferhat Abbas University

**Abderrahmane Menasria**

University of Khenchela

**Djamel Ghernaout**

University of Ha'il

**Malik Albrahim**

University of Ha'il

**Byong-Hun Jeon**

Hanyang University

**Hyun-Jo Ahn Ahn**

Hanyang University

**Yacine Benguerba**

Ferhat Abbas University

**Research Article**

**Keywords:** Higher-order shear deformation theory, artificial neural network, nonlocal parameter, nano-beam, porosity distribution

**Posted Date:** November 16th, 2026

**DOI:** https://doi.org/10.21203/rs.3.rs-11610632/v1

**License:** This work is licensed under a Creative Commons Attribution 4.0 International License.
Read Full License

**Additional Declarations:** No competing interests reported.

# HYBRID ANALYTICAL–ANN MODELLING OF FREE VIBRATION IN POROUS FUNCTIONALLY GRADED NANOBEAMS

**A. Bouhadra[2,3*], D. E. Lafi[1,3], A. Menasria[2,3], D. Ghernaout[4], M. Albrahim[4], B.-H. Jeon[5], H.-J. Ahn[5], and Y. Benguerba[6]**

[1]Civil Engineering Department, Faculty of Sciences and Technology, Ferhat Abbas University Sétif 1, 19000 Sétif, Algeria

[2]Civil Engineering Department, Faculty of Sciences and Technology, University of Khenchela, BP 1252 Road of Batna, 40000 Khenchela, Algeria

[3]Materials and Hydrology Laboratory, Civil Engineering Department, Faculty of Technology, University of Sidi Bel Abbes, BP 89, 22000 Sidi Bel Abbes, Algeria

[4]Chemical Engineering Department, College of Engineering, University of Ha'il, P.O. Box 2440, Ha'il 81441, Saudi Arabia

[5]Department of Earth Resources and Environmental Engineering, Hanyang University, 222 Wangsimni-ro, Seongdong-gu, Seoul 04763, Republic of Korea

[6]Laboratoire de Biopharmacie et Pharmacotechnie (LPBT), Ferhat Abbas University Sétif 1, 19000 Sétif, Algeria

***Keywords:*** *Higher-order shear deformation theory; artificial neural network; nonlocal parameter; nano-beam; porosity distribution.*

***Abstract.*** *This study investigates the dynamic analysis of functionally graded (FGM) nano-beams, accounting for porosity effects. The theoretical model is based on a higher-order shear deformation theory, integrated with Eringen's nonlocal elasticity and Hamilton's principle. The Navier solution provides an analytical framework for studying the free vibration behavior of these structures, whose material properties are assumed to vary continuously through the thickness. The proposed analytical model is first validated against existing results from the literature, showing excellent agreement. On this basis, an optimal Artificial Neural Network (ANN) is designed, trained, and tested using the analytical data. A comprehensive comparison is then conducted between the ANN predictions and the analytical model. The study also examines the influence of key parameters, including the material gradient index, nonlocal parameter, porosity distributions, geometric ratios, and the mechanical properties of the constituents (Young's modulus, density, and Poisson's ratio), on the nondimensional natural frequencies of the FGM nano-beams. The results confirm the robustness of the analytical formulation and underscore the effectiveness of the ANN as a reliable alternative tool for modeling the vibrational behavior of FGM nanostructures.*

## 1. Introduction

Recent advances in nanotechnology have stimulated growing interest in the study of nanometer-scale structures, particularly nano-beams, due to their outstanding mechanical performance and potential in high-

* Corresponding author; e-mail: abdelhakim.bouhadra@univ-khenchela.dz, tel.: [+213 669 058 481]

precision devices. Among the innovative materials used in such applications, functionally graded materials (FGMs) stand out for their ability to gradually combine the properties of two distinct phases, typically metallic and ceramic, in order to enhance the strength, durability, and thermal stability of structures. This continuous distribution of mechanical properties across the thickness introduces significant complexity into the modeling of dynamic behavior, especially in free vibration analysis [1-3]. At the same time, the rise of artificial intelligence (AI) has opened new perspectives for the modeling, prediction, and analysis of complex physical phenomena. In particular, artificial neural networks (ANNs) have emerged as powerful tools capable of capturing nonlinear relationships and approximating multivariate functions from experimental or numerical data. In this context, the integration of AI techniques into the vibrational study of FGM nanostructures represents a promising avenue to improve prediction accuracy while reducing the computational cost associated with traditional methods. This study lies within an interdisciplinary framework connected to emerging fields by proposing a hybrid approach that combines analytical modeling and machine learning to investigate the vibrational behavior of functionally graded (FG) nano-beams. The main objective is to develop a predictive model, based on neural networks, capable of accurately estimating the natural frequencies from geometric characteristics and material properties. The study particularly focuses on the influence of porosity models [4] and property variation laws, as well as on building a reliable and representative dataset to optimize network training.

Many researchers have recently integrated non-classical approaches (nonlocal theory [5], strain gradient theory [6, 7]) and artificial intelligence [8] to model the vibrational behavior of FG structures. Garg *et al.* [9] compared the performance of Gaussian process regression (GPR) and Random Forest (RF) models for predicting bending and buckling behavior of FGM nano-beams, revealing the superiority of GPR in terms of accuracy, even for unseen data. Cheng *et al.* [10] combined ANN with nonlocal strain gradient theory (NSGT) to analyze the natural frequencies of porous FGM nano-beams, highlighting the opposite effects of temperature gradients and nonlocal parameters, while characteristic length and porosity exhibited significant influence. Tariq *et al.* [11] proposed a semi-analytical solution based on nonlocal Levinson beam theory, integrating transverse springs and machine learning models (SVR/ANN), achieving highly accurate predictions ($R^2 \approx 1$) for gold nano-beams. Similarly, Zheng *et al.* [12] developed a hybrid analytical–ML model for rotating beams, showing that thickness effects increase vibration frequencies, while surface energy reduces them. From a more numerical perspective, Demir *et al.* [13] designed an ANN model under MATLAB for analyzing longitudinal vibrations of FGM bars, validated against FEM results obtained from SolidWorks. The integration of finite elements and AI has been further advanced by Mahesh [14], who developed a FEM–ANN model for porous functionally graded piezo-elasto-magnetic (PFG-PEM) plates, combining HSDT theory with Hamilton and von Karman equations to capture nonlinearities. Moreover, recent works by Jain and co-workers [15, 16] employed hybrid Rayleigh–Ritz/ANN approaches to model porous FGM plates on elastic foundations, achieving high accuracy for varying geometries. In the thermal domain, Wang *et al.* [17] applied a BP-ANN (back-propagation artificial neural network) coupled with a modified FEM to model the thermal vibration of 3D-FG microshells, emphasizing the importance of MLSP in countering thermal effects. Do *et al.* [18] combined deep neural networks (DNN) with the modified symbiotic organisms search (mSOS) algorithm to optimize material distribution in FG plates, surpassing traditional IGA approaches. Studies focusing on micro/nanostructures have also integrated NSGT: Lim *et al.* [19] proposed an advanced NSGT formulation with a modified internal energy kernel, later employed by Barati [20] and Aria *et al.* [21] to model forced vibrations and thermoelastic effects, respectively. Li *et al.* [22], followed by Tang *et al.* [23],

extended this theory to account for porosity and thickness effects on stiffness. Tang *et al.* [24] also investigated the influence of Poisson's ratio on thin nano-beams. In parallel, Eltaher *et al.* [25] demonstrated the impact of surface effects and porosity on the dynamic response of FGM beams using nonlocal FEM models. Experimental and numerical works, such as those by Ghazwani *et al.* [26], Saffari *et al.* [27] and Bouhadra *et al.* [28], have shown that the combined effects of porosity, material distribution, and nonlocal elasticity strongly influence natural frequencies.

Unlike existing studies that couple nonlocal elasticity with classical neural-network surrogates, the present work introduces a fully hybrid analytical–AI framework in which the analytical Higher-Order Shear Deformation Theory (HSDT) model provides a large, balanced database covering multiple porosity laws, nonlocal parameters, and material gradation indices. This hybridization ensures physically consistent learning, allowing the ANN to generalize beyond the analytical grid. In contrast to previous works [9-11] that treated porosity or nonlocality separately, our model simultaneously incorporates both effects and quantifies their coupled influence on the vibration response through statistical sensitivity analysis. Thus, this study provides a unified predictive framework bridging analytical mechanics and artificial intelligence for nano-scale FGM structures.

## 2. Mathematical Formulation

A supported FGM nano-beam is considered (length L, width b, thickness h – Fig. 1). Its Young's modulus (E) and mass density (ρ) follow a continuous distribution through the thickness according to a power-law, described by:

$$P(z) = P_m + (P_c - P_m)\left(\frac{z}{h} + \frac{1}{2}\right)^k \tag{1}$$

The effective mechanical properties, such as Young's modulus (E), Poisson's ratio (ν), and density (ρ)—are defined by the function P (z), where P (z) represents the effective property of the beam, Pc and Pm are the properties of the ceramic and metal phases, respectively, z is the coordinate along the thickness direction. K is the power-law index characterizing the FG material.

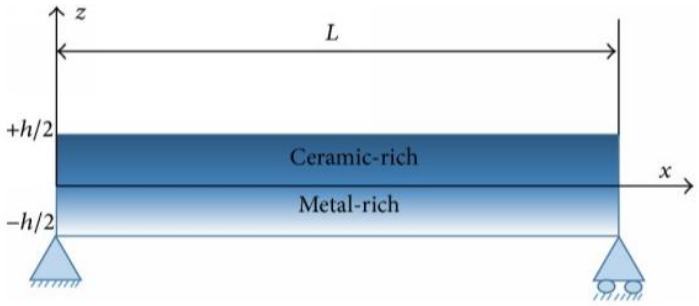



Fig. 1. A schematic of a functionally graded supported beam.

Five types of porosity models have been studied [29]: perfect model, imperfect model I, imperfect model II, imperfect model III, and imperfect model IV. The function characterizing the porosity can be expressed as follows:

*Perfect*
$$P(z) = P_m + (P_c - P_m)\left(\frac{z}{h} + \frac{1}{2}\right)^k \tag{2}$$

*Imperfect I*
$$P(z) = P_m + (P_c - P_m)\left(\frac{z}{h} + \frac{1}{2}\right)^k - \frac{\zeta}{2}(P_c + P_m) \tag{3}$$

*Imperfect II*
$$P(z) = P_m + (P_c - P_m)\left(\frac{z}{h} + \frac{1}{2}\right)^k - \frac{\zeta}{2}(P_c + P_m)\left(\frac{1-(z-1)}{h_0 - h_1}\right) \quad (4)$$

*Imperfect III*
$$P(z) = P_m + (P_c - P_m)\left(\frac{z}{h} + \frac{1}{2}\right)^k - \frac{\zeta}{2}(P_c + P_m)\left(\frac{1-|2z.(h_0 - h_1)|}{h_1 - h_0}\right) \quad (5)$$

*Imperfect IV*
$$P(z) = P_m + (P_c - P_m)\left(\frac{z}{h} + \frac{1}{2}\right)^k - \log\left(1 + \frac{\zeta}{2}\right)(P_c + P_m)\left(\frac{1-|2z-(h_0 - h_1)|}{h_1 - h_0}\right) \quad (6)$$

The porosity coefficient is defined by the symbol $\zeta$, where $0 \le \zeta \le 0.2$

### *2.1. Nonlocal elasticity theory*

According to Eringen's theory [5], the nonlocal constitutive equation is expressed as:

$$[1 - (e_0 a)^2 \nabla^2]\sigma_{kl} = \lambda \varepsilon_{rr}\delta_{kl} + \mu \varepsilon_{kl} \quad (7)$$

$\delta_{kl}$ : is the nonlocal stress tensor; $\boldsymbol{\varepsilon}_{kl}$: is the strain tensor; $\lambda$ and $\mu$ are Lamé's constants, $(e_0a)^2$ is a material constant, called the nonlocal parameter, in which $e_0$ is a material-specific constant, and is an internal characteristic length.

Thus, the nonlocal material response follows the constitutive form:

$$\sigma_{xx} - (e_o a)^2 \frac{\partial^2 \sigma_{xx}}{\partial x^2} = E\varepsilon_x, \quad \tau_{xz} - (e_o a)^2 \frac{\partial^2 \tau_{xz}}{\partial x^2} = G\gamma_{xz} \quad (8)$$

E is the Young's modulus (elasticity modulus); G = E/[2(1+ν)] is the shear modulus (where **ν** is Poisson's ratio); $\sigma_{xx}$ is the axial normal stress; $\sigma_{xz}$ is the shear stress; $\varepsilon_{xx}$ is the axial strain; and $\gamma_{xz}$ is the shear strain. When the nonlocal parameter is taken as $(e_0 a)^2 = 0$, the constitutive relation of local theory is recovered.

### *2.2. Kinematics and deformations*

The equilibrium equations governing the vibrational response of Functionally Graded Material (FGM) beams are derived using a Higher-order Shear Deformation Theory (HSDT). The total displacement field at any point in the structure can be expressed as follows.

$$\begin{aligned} u(x,y,z,t) &= u_0(x,t) - zw_{0,x}(x,t) + k_1 f(z)\int \theta(x,t)\,dx \\ w(x,z,t) &= w_0(x,t) \end{aligned} \quad (9)$$

$$k_1 = \lambda^2 \quad (10)$$

The new shape function $f(z)$ is proposed as follows:

$$f(z) = \frac{3\pi z}{25}\left[\pi - \sqrt[3]{0.135}\cosh\left(\frac{\pi z}{h}\right)\right], \quad g(z) = \frac{df(z)}{dz} \quad (11)$$

The kinematic relations can be obtained as follows:

$$\varepsilon_x = u_{0,x} + zk_x^b + f(z)k_x^s, \quad \{\gamma_{xz}\} = f'(z)\{\gamma_{xz}^0\} \quad (12)$$

With

$$\begin{Bmatrix} k_x^b \\ k_x^s \end{Bmatrix} = \begin{Bmatrix} -\dfrac{\partial^2 w_0}{\partial x^2} \\ k_1\theta \end{Bmatrix}, \quad \{\gamma_{xz}^0\} = \left\{k_1 \int \theta\, dx\right\} \quad (13)$$

The integrals used in the above equations shall be resolved by a Navier-type method and can be given as follows:

$$\frac{\partial}{\partial x}\int \theta \, dx = A'\frac{\partial^2 \theta}{\partial x^2}, \quad \int \theta \, dx = A'\frac{\partial \theta}{\partial x} \tag{14}$$

Where the coefficients $A'$ and $B'$ are expressed according to the type of solution used, in this case via Navier. Therefore, $A'$, $B'$, $k_1$ and $k_2$ are represented as follows:

$$A' = -\frac{1}{\lambda^2}, \quad \lambda = m\pi / a \tag{15}$$

***2.3. Constitutive relations***

The linear constitutive relations of an FG beam can be expressed:

For the first assumption (without the stretching effect), as:

$$\begin{Bmatrix} \sigma_x \\ \tau_{xz} \end{Bmatrix} = \begin{bmatrix} C_{11} & 0 \\ 0 & C_{55} \end{bmatrix} \begin{Bmatrix} \varepsilon_x \\ \gamma_{xz} \end{Bmatrix} \tag{16}$$

The $C_{ij}$ ($i, j = 1, 5.$) expressions in terms of engineering constants are given below:

$$C_{11} = E(z), \; C_{55} = G(z) = \frac{E(z)}{2(1+\nu)}. \tag{17}$$

The nonlocal constitutive relation for the macroscopic stress takes the following special relations for beams:

$$\sigma_x + \mu\frac{d^2\sigma_x}{dx^2} = C_{11}\varepsilon_x, \quad \tau_{xz} + \mu\frac{d^2\tau_{xz}}{dx^2} = C_{55}\gamma_{xz}; \qquad \mu = (e_0 a)^2 \tag{18}$$

Where E and G are Young's modulus and shear modulus, respectively; moreover, $e_0$ is a material constant, and $a$ is the internal characteristic length. Once the nonlocal parameter μ is equal to zero, we obtain the constitutive relations of the local theories.

***2.4. Equations of motion***

Hamilton's principle is used herein to derive the equations of motion. The principle can be stated in analytical form:

$$\int_{t_1}^{t_2} \delta(U - K)\, dt = 0 \tag{19}$$

In which $t_1$ and $t_2$ are the initial and end times, respectively. The change in the total strain energy is represented as follows:

$$\begin{aligned} \delta U &= \int_0^a \int_{h_{n-1}}^{h_n} \left(\sigma_x \delta\varepsilon_x + \tau_{xz}\delta\gamma_{xz}\right) dz\, dx \\ &= \int_0^a \begin{bmatrix} N_{xx}\dfrac{\partial \delta u_0}{\partial x} - M_{xx}\dfrac{\partial^2 \delta w_0}{\partial x^2} \\ -K_a A' P_{xx}\dfrac{\partial^2 \delta\theta}{\partial x^2} + Q_{xz}\left(K_a A'\dfrac{\partial \delta\theta}{\partial x} + \dfrac{\partial \delta\phi}{\partial x}\right) \end{bmatrix} dx \end{aligned} \tag{20}$$

Where $N_{xx}, M_{xx}, P_{xx}, N_{zz}$ and $Q_{xz}$ are the stress resultants, expressed as:

$$\left[N_x, M_{xx}, P_{xx}\right] = \sum_{n-1}^{3} \int_{h_{n-1}}^{h_n} \left[1,\ z, f(z)\right] \sigma_x \, dz \qquad Q_{xz} = \sum_{n-1}^{3} \int_{h_{n-1}}^{h_n} g(z)\, \tau_{xz} \, dz \tag{21}$$

;

*2.4.1. Mechanical constants*

$$\begin{aligned}
\left[A_{ij}, B_{ij}, D_{ij}\right] &= \sum_{n=1}^{3} \int_{h_n-1}^{h_n} Q_{ij}^{(n)}(z)\left[1, z, z^2\right] dz \\
\left[B_{sij}, D_{sij}, H_{sij}\right] &= \sum_{n=1}^{3} \int_{h_n-1}^{h_n} Q_{ij}^{(n)}(z)\left[f(z), zf(z), f(z)^2\right] dz \\
\left[L_{ij}, L_{ij}^{a}, R_{ij}\right] &= \sum_{n=1}^{3} \int_{h_n-1}^{h_n} Q_{ij}^{(n)}(z) g'(z)\left[1, z, f(z)\right] dz \\
\left[R_{ij}^{a}\right] &= \sum_{n=1}^{3} \int_{h_n-1}^{h_n} Q_{ij}^{(n)}(z)\left[g'(z)^2\right] dz \\
\left[A_{55}^{s}\right] &= \sum_{n=1}^{3} \int_{h_n-1}^{h_n} Q_{ij}^{(n)}(z)\left[g(z)^2\right] dz
\end{aligned} \tag{22}$$

The kinetic energy variation is represented as:

$$\delta K = \int_V \rho(z)\left(\dot{u}_0\, \delta\dot{u}_0 + \dot{w}_0\, \delta\dot{w}_0\right) dV$$

$$\delta K = \int_0^a \left[\begin{array}{l}
I_0\left(\dot{u}_0\, \delta\dot{u}_0 + \dot{w}_0 \delta\dot{w}_0\right) - I_1\left(\dot{u}_0 \dfrac{\partial \delta\dot{w}_0}{\partial x} + \dfrac{\partial \dot{w}_0}{\partial x}\delta\dot{u}_0\right) + I_2 \dfrac{\partial \dot{w}_0}{\partial x}\dfrac{\partial \delta\dot{w}_0}{\partial x} \\
-J_2 K_a A'\left(\dfrac{\partial \dot{w}_0}{\partial x}\dfrac{\partial \delta\dot{\theta}}{\partial x} + \dfrac{\partial \dot{\theta}}{\partial x}\dfrac{\partial \delta\dot{w}_0}{\partial x}\right) + J_1 K_a A'\left(\dot{u}_0 \dfrac{\partial \delta\dot{\theta}}{\partial x} + \dfrac{\partial \dot{\theta}}{\partial x}\delta\dot{u}_0\right) \\
+K_2\left(K_a A'\right)^2 \dfrac{\partial \dot{\theta}}{\partial x}\dfrac{\partial \delta\dot{\theta}}{\partial x} + J_0\left(\dot{w}_0 \delta\dot{\theta} + \dot{\theta}\delta\dot{w}_0\right) + K_0 \dot{\theta}\delta\dot{\theta}
\end{array}\right] dx \tag{23}$$

The dot–superscript convention is used to denote the time derivative.

$I_0, I_1, I_2, J_1, J_2, K_2, J_0$ and $K_0$ are the mass moments of inertia.

$$\left[I_0, I_2, I_3, I_4, J_1, J_2, K_1, K_2\right] = \int_{-h/2}^{+h/2} \rho(z)\left[1, z^2, z, f(z), g(z), zf(z), g^2(z), f^2(z)\right] dz \tag{24}$$

Substituting the expressions of $\delta U$, $\delta U_f$and $\delta K$ from Eqs. (20), (23) and (24) into Eq. (19), integrating by parts, and collecting the coefficients of $\delta u_0$, $\delta v_0$, $\delta w_0$, $\delta\theta$, and $\delta f_z$, the following equations of motion of the plate are obtained:

$$\begin{aligned}
\delta u_0 : &\quad N_{x,x} = \left(1 - \mu^2 \frac{\partial^2}{\partial x^2}\right)\left(I_0 \ddot{u}_0 - I_1 \frac{\partial \ddot{w}_0}{\partial x} - J_0 \frac{\partial \ddot{\theta}}{\partial x}\right) \\
\delta w_0 : &\quad M_{x,xx}^{b} = \left(1 - \mu^2 \frac{\partial^2}{\partial x^2}\right)\left(I_0 \ddot{w}_0 + I_1 \ddot{u}_{0,x} - I_2 \ddot{w}_{0,xx} - J_2 \ddot{\theta}_{,xx}\right) \\
\delta\theta : &\quad -k_1 M_x^{s} + k_1 A' S_{xz,x}^{s} = \left(1 - \mu^2 \frac{\partial^2}{\partial x^2}\right)\left(J_0 \ddot{u}_{0,x} - J_2 \ddot{w}_{0,xx} - K_2 \ddot{\theta}_{,xx}\right)
\end{aligned} \tag{25}$$

By substituting Eq. (21) into Eq. (25), the equations of motion can be expressed in terms of displacements ($\delta u_0$, $\delta v_0$, $\delta w_0$, $\delta\theta$, $\delta f_z$) as :

$$
\begin{aligned}
&A_{11}\frac{\partial^2 u_0}{\partial x^2}-B_{11}\frac{\partial^3 w_0}{\partial x^3}+B_{11}^s A'k_1\frac{\partial^3\theta}{\partial x^3}=\left(1-\mu^2\nabla^2\right)\left(I_0\ddot{u}_0-I_1\frac{\partial\ddot{w}_0}{\partial x}-J_0\frac{\partial\ddot{\theta}}{\partial x}\right)\\
&B_{11}\frac{\partial^3 u_0}{\partial x^3}-D_{11}\frac{\partial^4 w_0}{\partial x^4}+D_{11}^s A'k_1\frac{\partial^4\theta}{\partial x^4}=\\
&\left(1-\mu^2\frac{\partial^2}{\partial x^2}\right)\left(I_0\ddot{w}_0+I_1\frac{\partial\ddot{u}_0}{\partial x}-I_2\frac{\partial^2\ddot{w}_0}{\partial x^2}-J_2\frac{\partial^2\ddot{\theta}}{\partial x^2}\right)\\
&-B_{11}^s A'k_1\frac{\partial^3 u_0}{\partial x^3}+D_{11}^s A'k_1\frac{\partial^2 w_0}{\partial x^2}-H_{11}^s\left(A'k_1\right)^2\frac{\partial^2\theta}{\partial x^2}+A_{44}^s\left(A'k_1\right)^2\frac{\partial^2\theta}{\partial x^2}\\
&=\left(1-\mu^2\nabla^2\right)\left(J_0\frac{\partial\ddot{u}_0}{\partial x}-J_2\frac{\partial^2\ddot{w}_0}{\partial x^2}-K_2\frac{\partial^2\ddot{\theta}}{\partial x^2}\right)\\
&L(\frac{\partial u_0}{\partial x}+\frac{\partial v_0}{\partial y})-L^a(\frac{\partial^2 w_0}{\partial x^2}+\frac{\partial^2 w_0}{\partial y^2})-(R+A_{44}^s)\frac{\partial^2\theta}{\partial x^2}-(R+A_{55}^s)\frac{\partial^2\theta}{\partial y^2}=\left(1-\mu^2\frac{\partial^2}{\partial x^2}\right)J_1\ddot{w}_0
\end{aligned}
\tag{26}
$$

### *2.5. Exact solution for a simply supported FG beam*

Rectangular plates are generally classified according to the type of support used. This paper is concerned with the exact solutions of Eq. (26) for a simply supported FG beam. The following boundary conditions are imposed at the edges:

$$u_0=w_0=\theta=\frac{\partial\theta}{\partial x}=0 \qquad \text{at} \quad x=0,a \tag{27}$$

Following the Navier solution procedure, the authors assume the following solution from for $u_0$, $v_0$, $w_0$, $\theta$ and $f_z$ that satisfies the boundary conditions given in Eq. (27):

$$\begin{Bmatrix}u_0\\w_0\\\theta\end{Bmatrix}=\sum_{m=1}^{\infty}\begin{Bmatrix}U_m\cos(\pi\lambda)\\W_m\sin(\pi\lambda)\\\theta_m\sin(\pi\lambda)\end{Bmatrix}e^{i\omega t} \tag{28}$$

Where $U_m$, $V_{mn}$, $W_m$ and $\theta_m$ are arbitrary parameters to be determined, $\omega$ is the natural frequency.

The resulting operator equation is found as:

$$\left([K]-\left(1-\mu^2\nabla^2\right)[M]\omega^2\right)\{\Delta\}=\{0\} \tag{29}$$

With:

$$
\begin{aligned}
[K]&=\begin{bmatrix}-A_{11}\lambda^2 & B_{11}\lambda^3 & -K_aA'B_{11}^s\lambda^3\\ B_{11}\lambda^3 & -D_{11}\lambda^4-K_p\lambda^2-K_w\lambda & K_aA'D_{11}^s\lambda^4\\ -K_aA'B_{11}^s\lambda^3 & K_aA'D_{11}^s\lambda^4 & K_aA\left(H_{11}^s\lambda^4+A_{55}^s\lambda^2\right)\end{bmatrix}\\
[M]&=\begin{bmatrix}-I_0 & I_3\lambda^2 & K_1A'I_4\\ I_3\lambda^2 & -I_2\lambda^2-I_0 & -J_2\lambda^2\\ K_1A'I_4 & -J_2\lambda^2 & -K_2\lambda^2\end{bmatrix}
\end{aligned}
\tag{30}
$$

$$\{\Delta\}=\{U_m,W_m,\theta_m\}^T \tag{31}$$

The nondimensional frequencies used here have the following formula:

$$\varpi^2 = \omega L^2 \sqrt{\frac{\rho_U A}{E_U I}} \tag{32}$$

Where I=bh3 /12: is the moment of inertia of the cross-section of the beam

### 3. ANN Framework for Nano-Beam Vibration

In this study, several supervised learning techniques were explored to predict the natural frequencies of functionally graded (FGM) nanoplate structures, incorporating multiscale effects and material porosity. The tested methods include Bootstrap forest, Support Vector Machines (SVM), and Artificial Neural Networks (ANN). Among these approaches, ANNs demonstrated the best performance in modeling the complex relationships between the input parameters and the vibrational response of the system. The ANN model used (Fig. 2) is fully connected, with each neuron linked to all neurons in the next layer and nonlinear activation functions (such as ReLU, sigmoid, or hyperbolic tangent) applied. The input variables of the network include the mechanical properties of the FGM materials (such as Young's modulus and density), the slenderness ratio a/h, the scale factor, and the material index k, which describes the distribution of the ceramic and metallic phases through the thickness of the nano-beam. In addition, various porosity models (uniform, graded, and localized) were considered to reflect the actual imperfections in FGM structures, significantly influencing their effective mechanical properties.

A numerical database was generated by combining these parameters over a wide range of values. The corresponding natural frequencies were obtained using an accurate analytical model, which provided labeled data for training and validation. The entire process — data generation, analytical calculations, training, and testing of the neural network — was carried out entirely using the Maple software, leveraging its symbolic and numerical computing capabilities to develop a reliable predictive model for the vibration analysis of porous FGM nano-beams. The Artificial Neural Network (ANN) was implemented in *Maple* using a feed-forward architecture comprising one input layer, one hidden layer, and one output neuron. The hidden layer consisted of four neurons activated by the hyperbolic tangent (tanh) function, while the output layer employed a linear activation to predict the nondimensional frequency. The model was trained using the Levenberg–Marquardt optimization algorithm, with a learning rate of 0.01, batch size of 32, and a maximum of 1000 epochs. To prevent overfitting, an early-stopping criterion based on validation loss improvement (patience = 20 epochs) was applied. The performance was monitored using the Mean Squared Error (MSE) and the coefficient of determination ($R^2$).

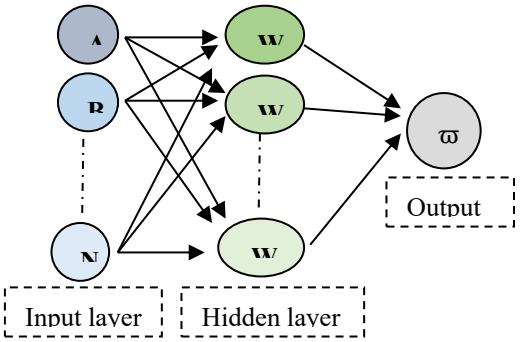



Fig. 2. The structuring of artificial neural networks to establish the objective function.

Table 1 presents the ranges of input variables considered for developing the supervised learning model. These ranges were selected to build an artificial neural network (ANN) model capable of predicting the nondimensional natural frequencies over a wide variety of nano-beam configurations made from different types

of functionally graded materials (FGMs), while accounting for nonlocal effects and material porosity. The material gradation index k varies from 0 to 10, the nonlocal scale parameter $(e_0a)^2$ ranges from 0 to 5, and the slenderness ratio (a/h) lies between 20 and 100. The effect of porosity is modeled using four different porosity distribution models (Models I, II, III, and IV), each representing a distinct distribution pattern within the material. For each model, several values of the porosity parameter $\xi=\{0.0, 0.1, 0.2\}$ are considered to capture various physical scenarios. A total of 3888 random combinations of input variables were generated within these ranges. For each set of inputs, an analytical method based on the higher-order shear deformation theory (HSDT) is used to compute the nondimensional vibration frequency, which is then used to label the data for training the ANN model. The complete dataset was divided into two subsets: 80% for training and 20% for validation.

TABLE 1. Input parameter ranges for machine learning models

| Input | | Range |
|---|---|---|
| K | | (0; 0.2; 0.5; 1.0; 5.0; 10.0) |
| $(e_0 a)^2$ | | (0; 1; 2; 3; 4; 5) |
| a/h | | (20; 50; 100) |
| $\zeta$ | | (0; 0.1; 0.2) |
| porosity models | | (Models I, II, III, and IV) |
| materials | steel alumina | $E_m = 210\,GPA,\ \nu_m = 0.3,\ \rho_m = 7800\,kg/m^3$<br>$E_c = 390\,GPA,\ \nu_c = 0.24,\ \rho_c = 3960\,kg/m^3$ |
| | AL alumina | $E_m = 70\,GPA,\ \nu_m = 0.3,\ \rho_m = 2707\,kg/m^3$<br>$E_c = 380\,GPA,\ \nu_c = 0.3,\ \rho_c = 3800\,kg/m^3$ |
| | SUS304 Si3N4 | $E_m = 207.79\,GPA,\ \nu_m = 0.3176,\ \rho_m = 8166\,kg/m^3$<br>$E_c = 322.27\,GPA,\ \nu_c = 0.24,\ \rho_c = 2370\,kg/m^3$ |
| | Ti-6Al-4V $ZrO_2$) | $E_m = 105.7\,GPA,\ \nu_m = 0.298,\ \rho_m = 4429\,kg/m^3$<br>$E_c = 151\,GPA,\ \nu_c = 0.3,\ \rho_c = 3000\,kg/m^3$ |

Based on the training set, various configurations of artificial neural networks (ANN) were tested by varying key hyperparameters such as batch size and the maximum number of epochs. The final selected model consists of a single hidden layer with four neurons. To assess the performance of the developed model, several evaluation metrics were applied to both the training and validation sets, including the coefficient of determination ($R^2$), the Root Mean Square Error (RMSE), and the mean squared error (MSE). The results in Table 2 obtained from the three predictive models (Artificial Neural Network, Bootstrap Forest, and Support Vector Machine) reveal notable differences in terms of accuracy and generalization ability. To benchmark the ANN's predictive ability, additional regression models—Gaussian Process Regression (GPR), Polynomial Regression (PR), and Response Surface Methodology (RSM)—were tested using the same dataset. The ANN consistently achieved the lowest RMSE and the highest $R^2$ values, outperforming traditional regression approaches that tend to underfit nonlinear coupling between kkk and $(e_0a)^2$. The quantitative comparison is summarized in Table 2.

TABLE 2. Evaluation metrics for the ANN model and other machine learning models

| Model | Validate on | $R^2$ | RMSE | MSE |
|---|---|---|---|---|
| ANN | Train set | 0.9959 | 0.1034 | 0.0107 |
| | Test set | 0.9957 | 0.1075 | 0.0115 |
| Bootstrap forest | Train set | 0.999 | 0.0516 | 0.0026 |
| | Test set | 0.998 | 0.0790 | 0.0062 |
| Support vector machine | Train set | 0.8136 | 0.7056 | 0.4979 |
| | Test set | 0.8086 | 0.7115 | 0.5062 |

The artificial neural network (ANN) demonstrates excellent performance, with a coefficient of determination $R^2$ of 0.9959 for the training set and 0.9957 for the test set. These values indicate the strong capability of the model to explain the variability in the data. Moreover, the prediction errors remain very low, with

RMSE values of 0.1034 (training) and 0.1075 (testing), and corresponding MSE values of 0.0107 and 0.0115. The consistency between the two phases highlights the model's good generalization capacity and robustness against overfitting. The Bootstrap Forest achieves the best overall performance. It reaches almost perfect accuracy, with $R^2$ values of 0.999 for training and 0.998 for testing.

Furthermore, its prediction errors are the lowest among all models, with RMSE values of 0.0516 (training) and 0.0790 (testing), along with very small MSE values (0.0026 and 0.0062). These results confirm the superior predictive power and stability of the Bootstrap Forest model. In contrast, the Support Vector Machine (SVM) shows significantly weaker performance. The $R^2$ values (0.8136 for training and 0.8086 for testing) remain much lower than those obtained with ANN and Bootstrap Forest. Similarly, the prediction errors are substantially higher (RMSE of 0.7056 and 0.7115; MSE of 0.4979 and 0.5062), indicating limited predictive accuracy and reduced suitability for this type of data. Overall, the Bootstrap Forest stands out as the most reliable and accurate model, followed closely by the ANN, while the SVM lags far behind. Globally, these results lead to the conclusion that the ANN neural network is a robust, accurate, and reliable tool for modeling the natural frequencies of functionally graded nano-beams (FGMs), even in the presence of heterogeneities or porosity.

The statistical analysis reveals that the material index k (Table 3) is by far the most influential parameter controlling the natural frequency of FGM nano-beams, with both its linear and quadratic contributions showing very strong effects. This highlights the crucial role of the compositional gradient in governing the dynamic response. The nonlocal parameter $(e_oa)^2$ also exhibits a very strong impact, confirming the significance of size-dependent effects at the nano-scale.

TABLE 3. Summary of the effects with corresponding Logworth and P-values

| Source | Logworth | P-value | Significance |
|---|---|---|---|
| k | 1020.908 | <0.00001 | Very strong |
| k*k | 460.539 | <0.00001 | Very strong |
| $(e_0a)^2$ | 323.676 | <0.00001 | Very strong |
| $\upsilon_m$*k | 79.048 | <0.00001 | strong |
| $\rho_c$*k | 31.533 | <0.00001 | strong |
| k*(eoa) $^2$ | 11.028 | <0.00001 | Moderate |
| Porosity model | 7.629–2.370 | <0.0001 to 0.00426 | Weak to moderate |
| $\rho_m$ | 0.464 | 0.34393 | ❌ Not significant |
| $\rho_m$* $\rho_c$ | 0.228 | 0.59188 | ❌ Not significant |
| $\rho_c$ | 0.080 | 0.83164 | ❌ Not significant |

Interactions such as $\nu_m \cdot k$ and $\rho_c \cdot k$ present strong influences, indicating that the Poisson's ratio of the metallic phase and the density of the ceramic phase act as important amplifiers of the gradient effect. The coupling term k $(e_oa)^2$shows a moderate contribution, suggesting that the combined action of material gradation and nonlocality should not be neglected. In contrast, the porosity model exhibits only a weak to moderate influence, while the isolated contributions of metal and ceramic densities remain statistically insignificant. Overall, the results demonstrate that the material gradation and nano-scale effects predominantly govern the vibrational behavior of FGM nano-beams, whereas porosity introduces only secondary modifications.

## 4. Numerical Results and Discussion

To validate the proposed method, Table 4 presents a comparison between the results obtained in this study and those reported by Eltaher *et al.* [30], who used the Euler–Bernoulli beam theory, as well as Rahmani and Pedram [31], who applied the Timoshenko beam theory. This comparison concerns functionally graded (FG) nano-

beams composed of a mixture of steel (metal phase) and alumina (ceramic phase). The mechanical properties of these materials, including Young's modulus, Poisson's ratio, and density, are defined as follows:

Steel: $$E_m = 210\,GPA,\ \nu_m = 0.3,\ \rho_m = 7800\,kg/m^3 \tag{33}$$

Alumina: $$E_c = 390\,GPA,\ \nu_c = 0.24,\ \rho_c = 3960\,kg/m^3 \tag{34}$$

The natural frequencies are nondimensionalized according to the following relation:

$$\varpi = \omega L^2 \sqrt{\frac{\rho_a S}{E_a I}} \tag{35}$$

Where $I = \frac{bh^3}{12}$ is the moment of inertia of the beam's cross-section.

The nondimensional natural frequencies of structures were investigated as a function of various parameters: the nonlocal parameter, the slenderness ratio (a/h), and the material distribution. The analysis was conducted under supported boundary conditions. Results were obtained using the Higher-order Shear Deformation Theory (HSDT) and an Artificial Neural Network (ANN). The current results (HSDT and ANN) show excellent agreement with available data in the literature. The maximum error between the results obtained by HSDT and ANN is 1.7%, with the majority of discrepancies being less than 1%. This convergence validates the robustness of the conclusions. The analysis reveals that an increase in the slenderness ratio (a/h) leads to a slight increase in the natural frequencies. Conversely, an increase in the nonlocal parameter or the power-law index causes a decrease in these frequencies. These trends are clearly illustrated and detailed in Table 4, demonstrating the complex interaction between material, geometric, and nonlocal properties on the vibrational behavior of the system.

TABLE 4. Validation and Comparison of Nondimensional Fundamental Natural Frequencies of Supported Nano-beams (steel alumina).

| L/h | $(e_0 a)^2$ | Source | | k=0 | k=0.2 | k=0.5 | k=1 | k=5 | k=10 |
|---|---|---|---|---|---|---|---|---|---|
| 20 | 0 | Eltaher *et al.* [30] | | 9.8797 | 8.72 | 7.8061 | 7.0904 | 6.0025 | 5.7058 |
| | | Rahmani and Pedram [31] | | 9.8296 | 8.66 | 7.7149 | 6.9676 | 5.9172 | 5.6521 |
| | | Present | HSDT | 9.8293 | 8.6599 | 7.7151 | 6.9677 | 5.9165 | 5.6514 |
| | | | ANN | 9.7735 | 8.6756 | 7.7505 | 7.0213 | 5.9193 | 5.6611 |
| | | Abs Error (HSDT vs. ANN) in % | | 0.57% | 0.18% | 0.46% | 0.76% | 0.05% | 0.17% |
| | 1 | Eltaher *et al.* [30] | | 9.4238 | 8.3175 | 7.4458 | 6.7631 | 5.7256 | 5.4425 |
| | | Rahmani and Pedram [31] | | 9.3777 | 8.262 | 7.3602 | 6.6473 | 5.6452 | 5.3923 |
| | | Present | HSDT | 9.3777 | 8.2619 | 7.3606 | 6.6476 | 5.6444 | 5.3915 |
| | | | ANN | 9.3697 | 8.3127 | 7.4229 | 6.7227 | 5.6644 | 5.4135 |
| | | Abs Error (HSDT vs. ANN) in % | | 0.09% | 0.61% | 0.84% | 1.12% | 0.35% | 0.41% |
| | 2 | Eltaher *et al.* [30] | | 9.0257 | 7.9661 | 7.1312 | 6.4774 | 5.4837 | 5.2126 |
| | | Rahmani and Pedram [31] | | 8.9829 | 7.914 | 7.0504 | 6.3674 | 5.4075 | 5.1653 |
| | | Present | HSDT | 8.983 | 7.9144 | 7.0508 | 6.3677 | 5.4066 | 5.1644 |
| | | | ANN | 8.987 | 7.9694 | 7.1136 | 6.4412 | 5.424 | 5.1795 |
| | | Abs Error (HSDT vs. ANN) in % | | 0.04% | 0.69% | 0.88% | 1.14% | 0.32% | 0.29% |
| | 3 | Eltaher *et al.* [30] | | 8.6741 | 7.6557 | 6.8533 | 6.2251 | 5.2702 | 5.0096 |
| | | Rahmani and Pedram [31] | | 8.6341 | 7.6068 | 6.7766 | 6.1202 | 5.1975 | 4.9647 |
| | | Present | HSDT | 8.6341 | 7.6069 | 6.7768 | 6.1204 | 5.1969 | 4.9639 |
| | | | ANN | 8.6246 | 7.6451 | 6.8221 | 6.1764 | 5.1978 | 4.9587 |
| | | Abs Error (HSDT vs. ANN) in % | | 0.11% | 0.50% | 0.66% | 0.91% | 0.02% | 0.10% |
| | 4 | Eltaher *et al.* [30] | | 8.3607 | 7.3791 | 6.6057 | 6.0001 | 5.0797 | 4.8286 |
| | | Rahmani and Pedram [31] | | 8.323 | 7.3327 | 6.5325 | 5.8997 | 5.0103 | 4.7858 |
| | | Present | HSDT | 8.3228 | 7.3329 | 6.5328 | 5.8999 | 5.0097 | 4.7852 |

| L/h | $(e_0 a)^2$ | Source | | k=0 | k=0.2 | k=0.5 | k=1 | k=5 | k=10 |
|---|---|---|---|---|---|---|---|---|---|
| | | | ANN | 8.2818 | 7.339 | 6.5476 | 5.9275 | 4.9851 | 4.7505 |
| | | Abs Error (HSDT vs. ANN) in % | | 0.50% | 0.08% | 0.23% | 0.47% | 0.49% | 0.73% |
| | 5 | Eltaher *et al.* [30] | | 8.0789 | 7.1303 | 6.383 | 5.7979 | 4.9086 | 4.6659 |
| | | Rahmani and Pedram [31] | | 8.0433 | 7.0863 | 6.3129 | 5.7014 | 4.8419 | 4.625 |
| | | Present | HSDT | 8.0433 | 7.0866 | 6.3135 | 5.702 | 4.8413 | 4.6246 |
| | | | ANN | 7.9579 | 7.0504 | 6.2894 | 5.6939 | 4.7854 | 4.5544 |
| | | Abs Error (HSDT vs. ANN) in % | | 1.07% | 0.51% | 0.38% | 0.14% | 1.17% | 1.54% |
| 50 | 0 | Eltaher *et al.* [30] | | 9.8724 | 8.7115 | 7.7998 | 7.0852 | 5.999 | 5.7001 |
| | | Rahmani and Pedram [31] | | 9.8631 | 8.6895 | 7.7413 | 6.9917 | 5.9389 | 5.673 |
| | | Present | HSDT | 9.8629 | 8.6896 | 7.7414 | 6.9916 | 5.9389 | 5.6728 |
| | | | ANN | 9.7874 | 8.689 | 7.7635 | 7.034 | 5.9309 | 5.6716 |
| | | Abs Error (HSDT vs. ANN) in % | | 0.77% | 0.01% | 0.29% | 0.61% | 0.14% | 0.02% |
| | 1 | Eltaher *et al.* [30] | | 9.4172 | 8.3114 | 7.4403 | 6.7583 | 5.7218 | 5.4389 |
| | | Rahmani and Pedram [31] | | 9.4097 | 8.2901 | 7.3854 | 6.6703 | 5.6659 | 5.4122 |
| | | Present | HSDT | 9.4094 | 8.29 | 7.3853 | 6.6704 | 5.6656 | 5.412 |
| | | | ANN | 9.3832 | 8.3257 | 7.4355 | 6.735 | 5.6755 | 5.4235 |
| | | Abs Error (HSDT vs. ANN) in % | | 0.28% | 0.43% | 0.68% | 0.97% | 0.17% | 0.21% |
| | 2 | Eltaher *et al.* [30] | | 9.0205 | 7.9613 | 7.1269 | 6.4737 | 5.4808 | 5.2098 |
| | | Rahmani and Pedram [31] | | 9.0136 | 7.9411 | 7.0745 | 6.3895 | 5.4274 | 5.1843 |
| | | Present | HSDT | 9.0134 | 7.9408 | 7.0745 | 6.3896 | 5.4272 | 5.184 |
| | | | ANN | 9.0002 | 7.9821 | 7.126 | 6.4533 | 5.4348 | 5.1891 |
| | | Abs Error (HSDT vs. ANN) in % | | 0.15% | 0.52% | 0.73% | 1.00% | 0.14% | 0.10% |
| | 3 | Eltaher *et al.* [30] | | 8.67 | 7.652 | 6.85 | 6.2222 | 5.2679 | 5.0074 |
| | | Rahmani and Pedram [31] | | 8.6636 | 7.6327 | 6.7998 | 6.1414 | 5.2166 | 4.983 |
| | | Present | HSDT | 8.6633 | 7.6327 | 6.7999 | 6.1415 | 5.2163 | 4.983 |
| | | | ANN | 8.6375 | 7.6575 | 6.8342 | 6.1882 | 5.2082 | 4.9679 |
| | | Abs Error (HSDT vs. ANN) in % | | 0.30% | 0.33% | 0.50% | 0.76% | 0.16% | 0.30% |
| | 4 | Eltaher *et al.* [30] | | 8.3575 | 73,762 | 6.6031 | 5.9979 | 5,078 | 4.8269 |
| | | Rahmani and Pedram [31] | | 8.3515 | 73,577 | 6.5548 | 5.9201 | 50,287 | 4.8035 |
| | | Present | HSDT | 8.3511 | 7.3574 | 6.5548 | 5.9199 | 5.0285 | 4.8032 |
| | | | ANN | 8.2945 | 7.3511 | 6.5594 | 5.9391 | 4.9952 | 4.7593 |
| | | Abs Error (HSDT vs. ANN) in % | | 0.68% | 0.09% | 0.07% | 0.32% | 0.66% | 0.91% |
| | 5 | Eltaher *et al.* [30] | | 8.0765 | 7.1282 | 6.3811 | 5.7962 | 4.9072 | 4.6646 |
| | | Rahmani and Pedram [31] | | 8.0708 | 7.1104 | 6.3345 | 5.7212 | 4.8597 | 4.6421 |
| | | Present | HSDT | 8.0705 | 7.1103 | 6.3346 | 5.721 | 4.8596 | 4.6419 |
| | | | ANN | 7.9702 | 7.0623 | 6.301 | 5.7052 | 4.7953 | 4.5628 |
| | | Abs Error (HSDT vs. ANN) in % | | 1.24% | 0.68% | 0.53% | 0.28% | 1.32% | 1.70% |
| 100 | 0 | Eltaher *et al.* [30] | | 9.8696 | 8.711 | 7.798 | 7.083 | 5.997 | 5.7005 |
| | | Rahmani and Pedram [31] | | 9.868 | 8.6938 | 7.7451 | 6.9952 | 5.9421 | 5.676 |
| | | Present | HSDT | 9.8677 | 8.6937 | 7.7449 | 6.9951 | 5.942 | 5.6758 |
| | | | ANN | 9.8107 | 8.7115 | 7.7853 | 7.0553 | 5.9502 | 5.6891 |
| | | Abs Error (HSDT vs. ANN) in % | | 0.58% | 0.20% | 0.52% | 0.86% | 0.14% | 0.23% |
| | 1 | Eltaher *et al.* [30] | | 9.4162 | 8.3106 | 7.4396 | 6.7577 | 5.7212 | 5.4384 |
| | | Rahmani and Pedram [31] | | 9.4143 | 8.2941 | 7.3891 | 6.6736 | 5.6689 | 5.415 |
| | | Present | HSDT | 9.4145 | 8.294 | 7.389 | 6.6735 | 5.6688 | 5.4149 |
| | | | ANN | 9.4059 | 8.3476 | 7.4567 | 6.7558 | 5.6942 | 5.4402 |
| | | Abs Error (HSDT vs. ANN) in % | | 0.09% | 0.65% | 0.92% | 1.23% | 0.45% | 0.47% |

| L/h | $(e_0 a)^2$ | Source | | k=0 | k=0.2 | k=0.5 | k=1 | k=5 | k=10 |
|---|---|---|---|---|---|---|---|---|---|
| | 2 | Eltaher *et al.* [30] | | 9.0197 | 7.9607 | 7.1263 | 6.4731 | 5.4803 | 5.2094 |
| | | Rahmani and Pedram [31] | | 9.018 | 7.9449 | 7.078 | 6.3927 | 5.4302 | 5.1871 |
| | | Present | HSDT | 9.0178 | 7.9449 | 7.0779 | 6.3925 | 5.4301 | 5.187 |
| | | | ANN | 9.0223 | 8.0034 | 7.1467 | 6.4735 | 5.4529 | 5.2051 |
| | | Abs Error (HSDT vs. ANN) in % | | 0.05% | 0.74% | 0.97% | 1.27% | 0.42% | 0.35% |
| | 3 | Eltaher *et al.* [30] | | 8.6695 | 7.6515 | 6.8496 | 6.2217 | 5.2675 | 5.0071 |
| | | Rahmani and Pedram [31] | | 8.6678 | 7.6365 | 6.8032 | 6.1444 | 5.2194 | 4.9857 |
| | | Present | HSDT | 8.6677 | 7.6364 | 6.8031 | 6.1444 | 5.2193 | 4.9856 |
| | | | ANN | 8.6592 | 7.6783 | 6.8544 | 6.2079 | 5.2257 | 4.9833 |
| | | Abs Error (HSDT vs. ANN) in % | | 0.10% | 0.55% | 0.75% | 1.03% | 0.12% | 0.05% |
| | 4 | Eltaher *et al.* [30] | | 8.3571 | 7.3758 | 6.6028 | 5.9976 | 5.0777 | 4.8267 |
| | | Rahmani and Pedram [31] | | 8.3555 | 7.3613 | 6.558 | 5.9231 | 5.0313 | 4.806 |
| | | Present | HSDT | 8.3554 | 7.3612 | 6.5579 | 5.9229 | 5.0312 | 4.8059 |
| | | | ANN | 8.3156 | 7.3715 | 6.5792 | 5.9584 | 5.0123 | 4.7741 |
| | | Abs Error (HSDT vs. ANN) in % | | 0.48% | 0.14% | 0.32% | 0.60% | 0.38% | 0.66% |
| | 5 | Eltaher *et al.* [30] | | 8.0762 | 7.1279 | 6.3808 | 5.796 | 4.9071 | 4.6644 |
| | | Rahmani and Pedram [31] | | 8.0747 | 7.1139 | 6.3376 | 5.724 | 4.8623 | 4.6445 |
| | | Present | HSDT | 8.0745 | 7.1138 | 6.3376 | 5.7239 | 4.8621 | 4.6444 |
| | | | ANN | 7.9909 | 7.0823 | 6.3204 | 5.7242 | 4.8119 | 4.577 |
| | | Abs Error (HSDT vs. ANN) in % | | 1.04% | 0.44% | 0.27% | 0.01% | 1.03% | 1.45% |

Fig. 3 illustrates the variation of dimensionless frequency ($\bar{\omega}$) with the material index (k) for various composite materials, comparing results from HSDT theory and Artificial Neural Networks (ANN) under specific conditions (a/h=50 and $(e_0.a)^2$=0). The HSDT and ANN curves show remarkable overlap, validating the robustness of the ANN model. For all materials, an increase in the material index (k) leads to a significant decrease in the dimensionless frequency, particularly pronounced at low k values. Furthermore, materials such as "Steel Alumina/$Al_2O_3$" and "AL alumina" generally exhibit higher dimensionless frequencies than their counterparts, highlighting the predominant influence of material type on the system's vibrational response.

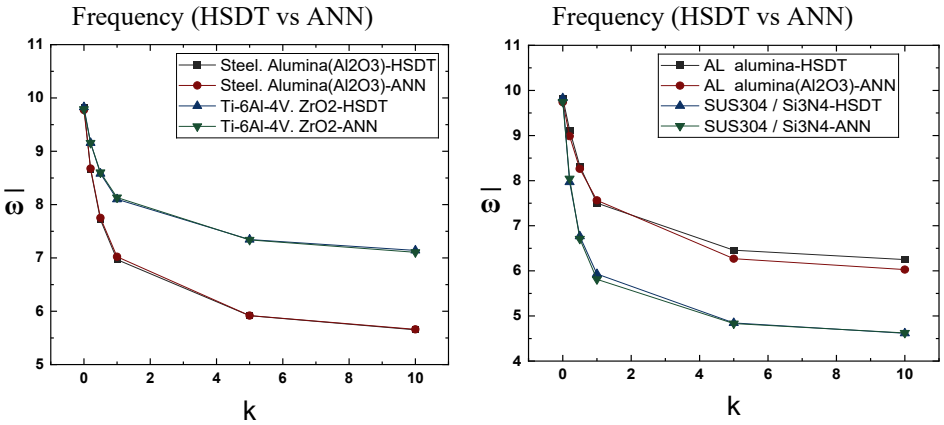



Fig. 3. Effect of Material Index on Dimensionless Frequency in Various Composites: HSDT and ANN Results (a/h=50, $(e_0.a)^2$=0, Steel alumina).

Fig. 4 provides compelling visual evidence that both the material index and the nonlocal parameter play critical roles in determining the dimensionless natural frequencies of the system. Specifically, an increase in either of these parameters leads to a reduction in the system's natural frequencies, with nonlocal effects consistently contributing to a softening behavior.

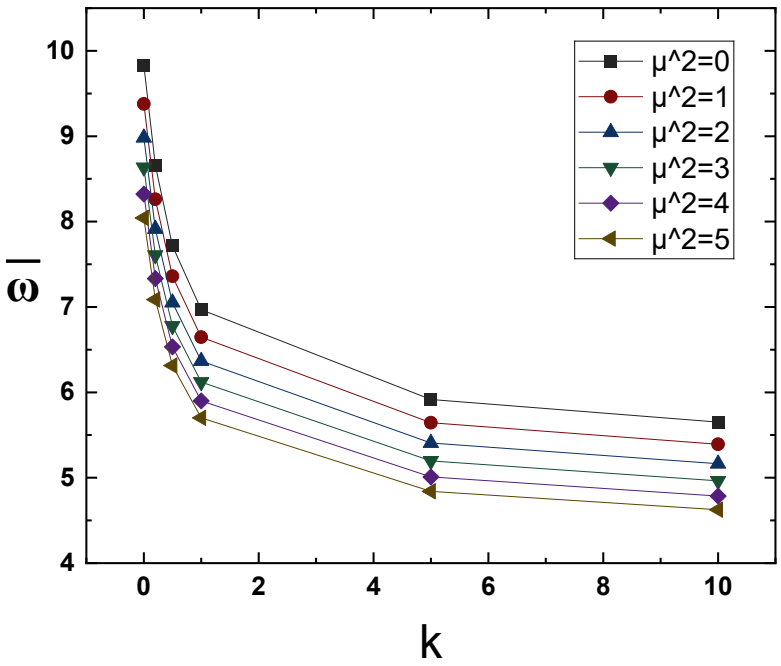



Fig. 4. Interdependence of Dimensionless Frequency, Material Index, and Nonlocal Parameter ($\mu^2=(e_0.a)^2$) (a/h=50; Steel Alumina ).

Fig. 5 (comprising multiple sub-graphs) illustrates the multi-factorial impact of the porosity parameter (ξ), the material index (k), and the nonlocal parameter $(e_oa)^2$ on the dimensionless frequency ($\bar{\omega}$), at a constant slenderness ratio (a/h=50). Each sub-graph represents an increasing value of the nonlocal parameter.

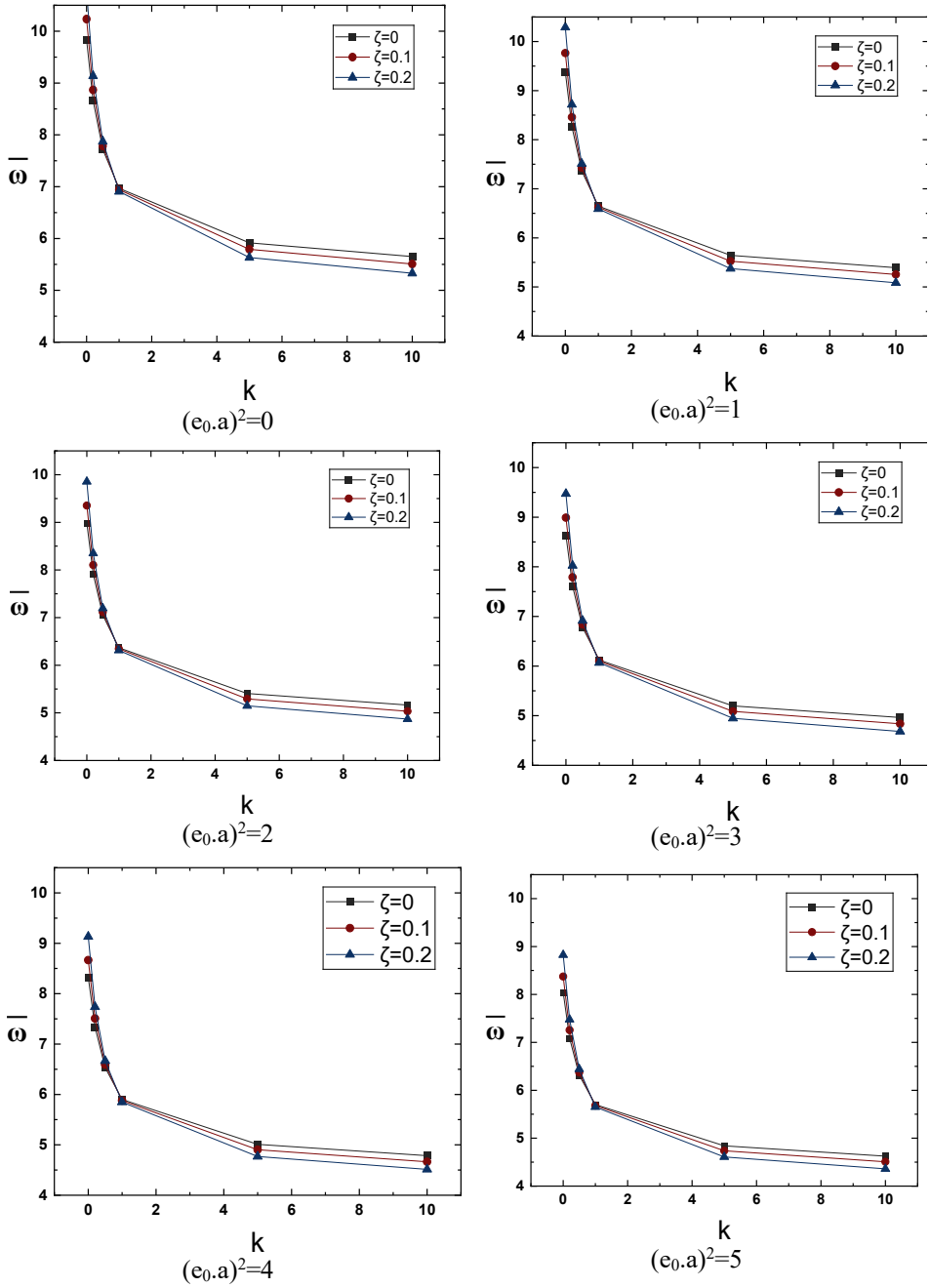



Fig. 5. Dimensionless frequency variation as a function of porosity parameter ξ, material index k, and nonlocal parameter $(e_0.a)^2$ (a/h=50; Steel alumina).

It is consistently observed that an increase in the material index (k) leads to a decrease in frequencies, particularly pronounced at low k values. Simultaneously, an increase in the porosity parameter (ξ) causes a reduction in dimensionless frequencies, indicating a softening of the system. Finally, the effect of the nonlocal parameter manifests as a general decrease in frequencies as its value increases, consistent with previous observations. This figure highlights the complex interaction and synergistic behavior of these three parameters on the vibrational response of the structure. The nonlocal parameter $(e_0a)^2$ reflects the **internal length-scale dependency** at the nano-scale, introducing a size-effect that softens the structure by accounting for long-range interatomic interactions. As this parameter increases, the effective stiffness decreases, leading to lower natural frequencies. This trend is consistent with Eringen's theory, where stress at a point depends not only on local strain

but also on the strain field in its neighborhood. Fig. 6, comprising four sub-graphs, analyzes the variation of dimensionless frequency ($\varpi$) as a function of the material index (k).

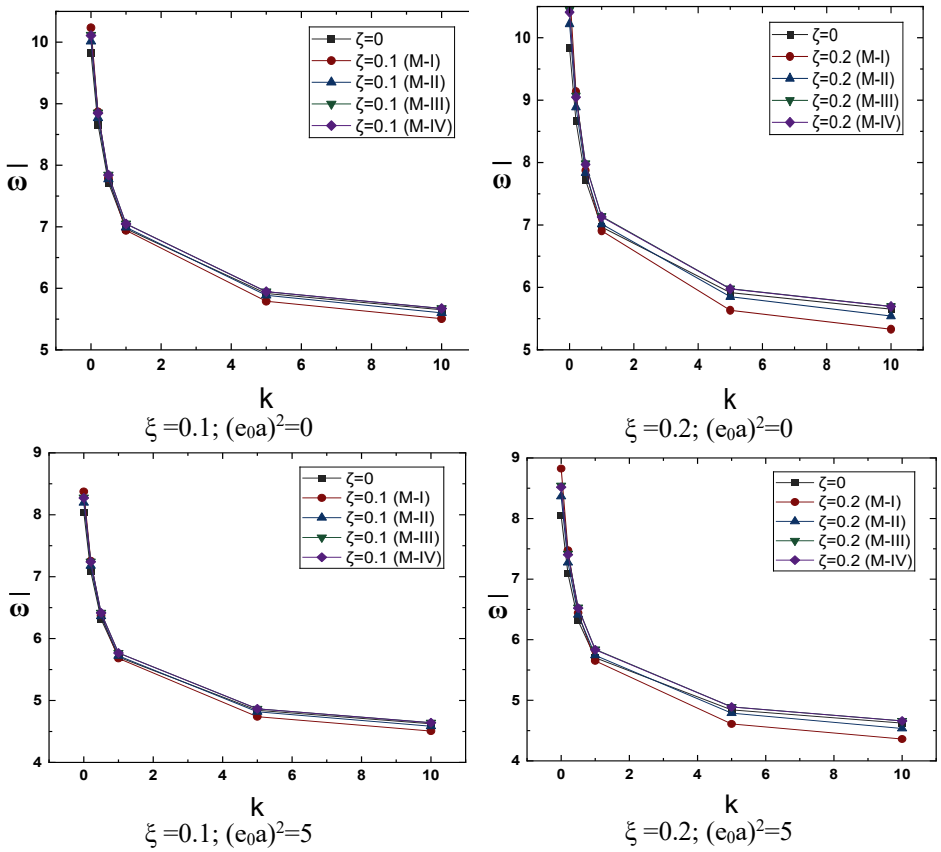



Fig. 6. Dimensionless frequency variation as a function of the material index k, nonlocal parameter $(e_0.a)^2$, and imperfect porosity patterns ξ (a/h=50; Steel alumina).

This investigation is conducted for two distinct values of the nonlocal parameter $(e_oa)^2$ and critically highlights the influence of the perfect model (no porosity, ξ=0) and four imperfect porosity models (M-I to M-IV), while maintaining a constant slenderness ratio (a/h=50). Each sub-graph details the results for a specific porosity level (ξ) and nonlocal parameter. A general trend of decreasing frequency is observed with increasing material index (k) across all scenarios. Notably, the perfect model and the four imperfect porosity models induce slightly distinct frequencies, with more pronounced divergences at certain k values. Furthermore, an increase in the nonlocal parameter leads to an overall reduction in frequencies, indicating a softening of the system. This analysis underscores the importance of not only the presence and degree of porosity but also its modeling in determining the vibrational behavior of the structure. Fig. 7 presents the variation of dimensionless frequency ($\bar{\omega}$) as a function of the material index (k) for four distinct composites, under fixed conditions (a/h=50, $(e_0a)^2$=0).

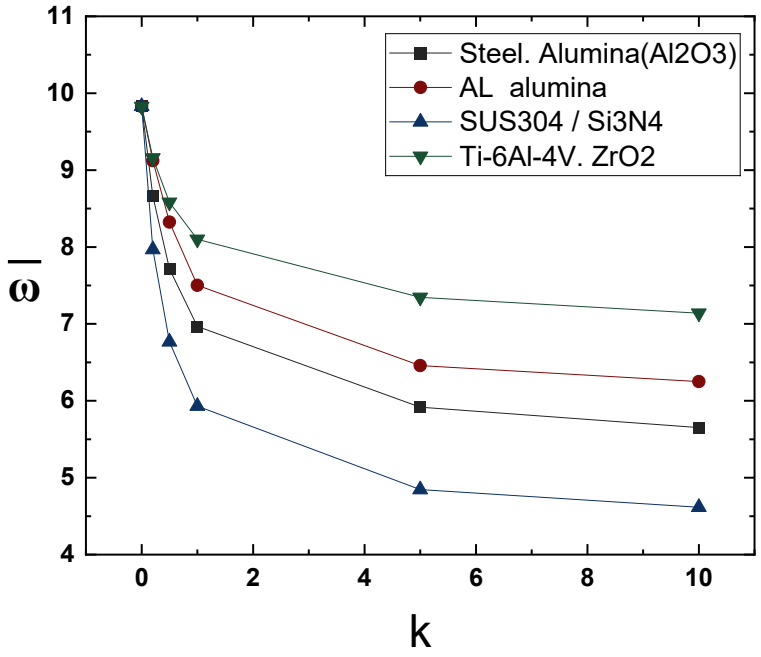



Fig. 7. Dimensionless frequency variation as a function of the material index k (a/h=50 ; $(e_0.a)^2$=0).

For all materials, a significant decrease in $\bar{\omega}$ is observed as k increases. A crucial observation is that at low k values (approximately k≤0.5), the frequencies of the four materials are very close. However, beyond this range, a marked and increasing divergence appears among them. "Steel Alumina" maintains the highest frequencies, while "Ti-6Al-4V/ZrO2" shows the lowest. This trend highlights that the impact of the material type on the vibrational response becomes predominant with increasing material heterogeneity. Fig. 8 illustrates the variation of dimensionless frequency (ANN) with Young's moduli of metal ($E_m$) and ceramic (Ec). In these plots, with k=10 (a/h=20), contour lines represent equal frequencies. It's observed that increasing either Ec or Em generally tends to decrease the dimensionless frequency (ANN). Comparing the figures also reveals the impact of parameters ξ and $(e_0a)^2$. An increase in ξ from 0.0 to 0.2 (for $(e_0a)^2$=0) leads to a noticeable reduction in frequencies. These results are crucial for optimizing the design of FGM (metal-ceramic) composites based on specific vibrational requirements.

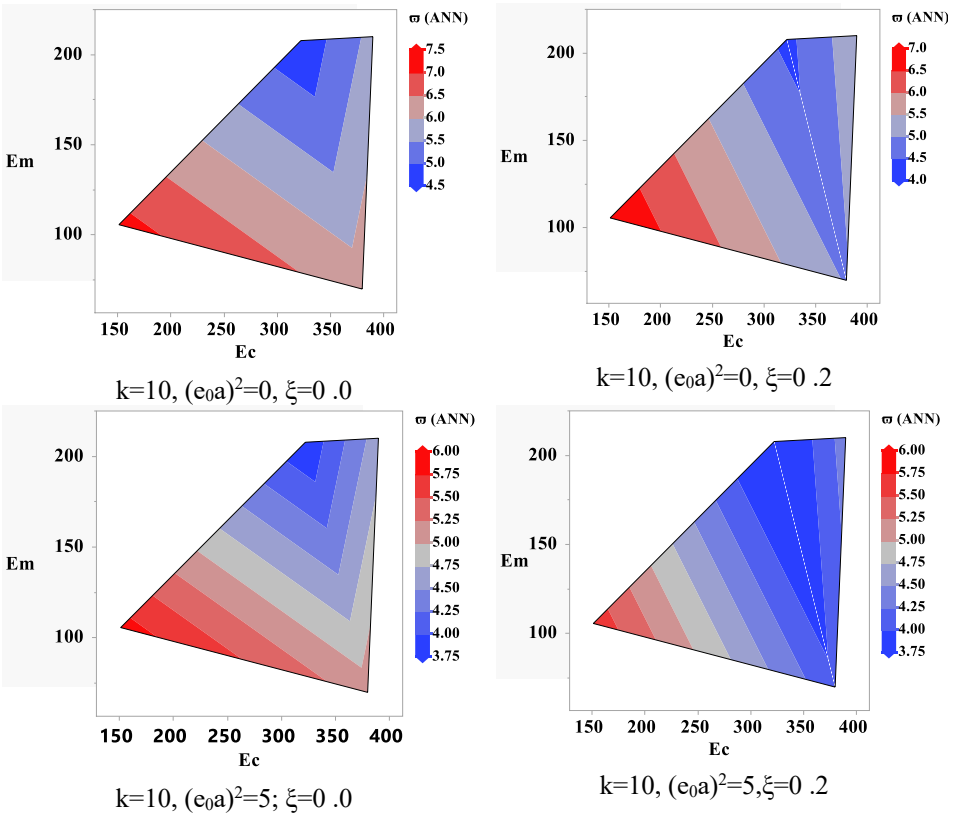



Fig. 8. Dimensionless frequency variation as a function of $E_m$ and $E_c$, and parameter $(e_oa)^2$ (k=10: a/h=20).

Fig. 9 displays the variation of dimensionless frequency (ANN) with metal ($\rho_m$) and ceramic ($\rho_c$) densities. For k=10 (a/h=20), contour lines represent equal frequencies. It is consistently observed that increasing either ρc or ρm leads to a decrease in the dimensionless frequency (ANN). Comparing the graphs reveals that increasing the parameter ξ (from 0.0 to 0.2) significantly lowers the overall frequency. These findings are crucial for designing FGM (metal-ceramic) composites where vibrational properties depend on material densities.

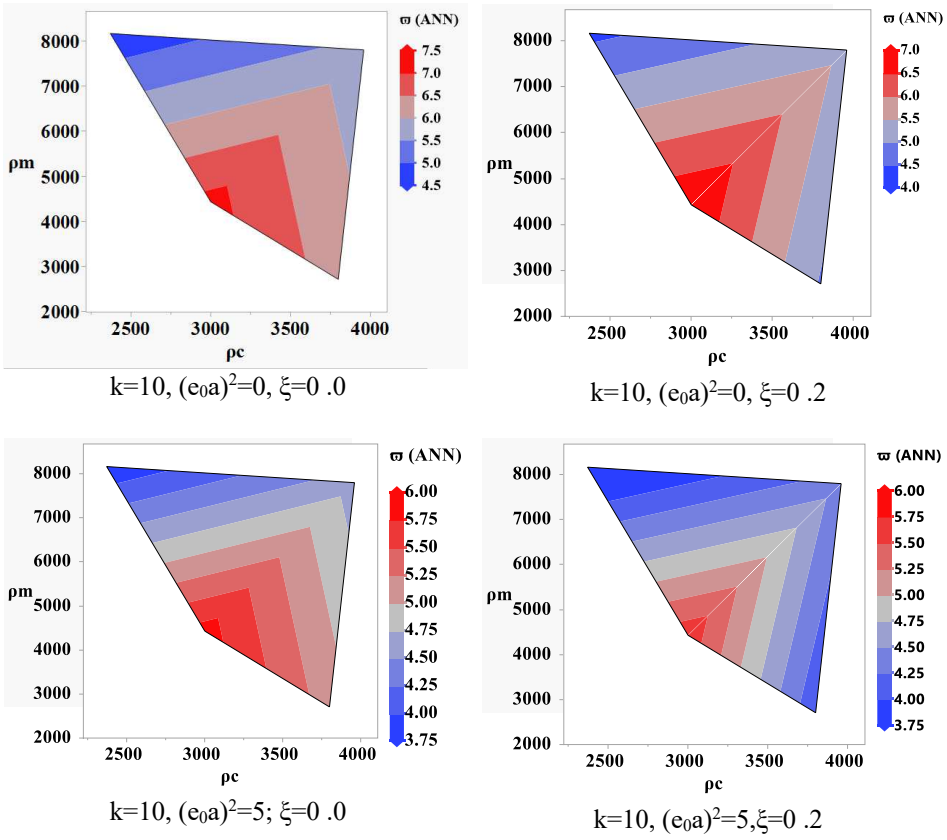



Fig. 9. Dimensionless frequency variation (ANN) as a function of $\rho$m and $\rho$c, and the parameter $(e_oa)^2$ (k=10, a/h=20).

Fig. 10 and 11 illustrate the variation of dimensionless frequency (ANN) with various parameters, whose effects are statistically very significant on the response variable. Fig. 10 shows that frequency (ANN) generally decreases with increasing ceramic density ($\rho_c$) and the parameter $(e_0a)^2$, with a notable drop due to increasing $\xi$ from 0.0 to 0.2.

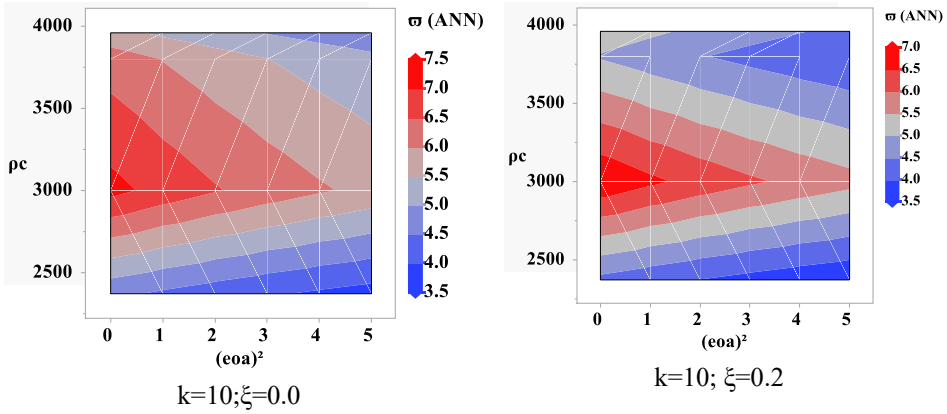
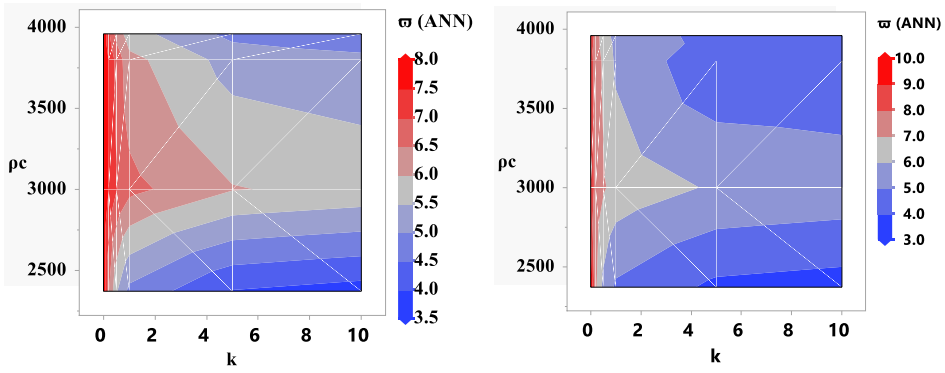



Fig. 10. Dimensionless frequency variation (ANN) as a function of ρc, and the parameter $(e_oa)^2$ (k=10, a/h=20).

Fig. 11, for $(e_0a)^2$=5, reveals a significant decrease in frequency (ANN) as $\rho_m$ increases. Furthermore, it highlights that frequency drastically decreases with increasing the ratio k. These plots are crucial for the optimized design of FGM (metal-ceramic) composites.




$(e_0a)^2=5;\xi=0.0$ $(e_0a)^2=5,\xi=0.2$

Fig. 11. Dimensionless frequency variation (ANN) as a function of ρm and K, ($(e_oa)^2=5$, a/h=20).

## 5. Conclusions

This study developed a hybrid analytical–ANN framework for predicting the free vibration behavior of porous functionally graded nano-beams. The analytical model, based on Higher-Order Shear Deformation Theory (HSDT) and Eringen's nonlocal elasticity, generated a comprehensive dataset encompassing variations in material gradation, porosity, and geometric ratios. The trained ANN achieved excellent predictive accuracy ($R^2 \approx 0.996$; RMSE ≈ 0.10), reducing the computational time by nearly 95 % compared with full analytical sweeps.

Parametric analysis revealed that the material index k and nonlocal parameter $(e_0a)^2$ dominate the vibrational response, while porosity effects are secondary but non-negligible. The hybrid approach bridges continuum mechanics and data-driven modeling, enabling rapid and reliable prediction of nano-scale vibrational properties without re-solving the full governing equations.

Future extensions will integrate finite-element verification, physics-informed neural networks (PINNs), and uncertainty quantification, thereby enhancing generalization and applicability to complex boundary and loading conditions.

**Statements and Declarations**

**Funding.** [The authors declare that no funds, grants, or other support were received during the preparation of this manuscript.]

**Competing interests.** [The authors have no relevant financial interests to disclose]

**Author contributions.** A. Bouhadra: conceptualization, methodology, writing – original draft; D. E. Lafi: software, formal analysis; … All authors read and approved the final manuscript.

**Data availability.** The datasets generated and analysed during the current study are available from the corresponding author on reasonable request.

## REFERENCES

1. Chen D, Kitipornchai S, Yang J. Nonlinear free vibration of shear deformable sandwich beam with a functionally graded porous core. Thin-Walled Struct. 2016;107:39-48. https://doi.org/10.1016/j.tws.2016.05.025
2. Lv Z, Qiu Z, Zhu J, Zhu B, Yang W. Nonlinear free vibration analysis of defective FG nanobeams embedded in elastic medium. Compos Struct. 2018;202:675-85. https://doi.org/10.1016/j.compstruct.2018.03.068
3. Adiyaman G. Free vibration analysis of a porous 2D functionally graded beam using a high-order shear deformation theory. J Vib Eng Technol. 2024;12(2):2499-516. https://doi.org/10.1007/s42417-023-00996-4

4. Chen D, Yang J, Kitipornchai S. Elastic buckling and static bending of shear deformable functionally graded porous beam. Compos Struct. 2015;133:54-61. https://doi.org/10.1016/j.compstruct.2015.07.052
5. Eringen AC. Nonlocal Continuum Field Theories. New York: Springer; 2002.
6. Mindlin RD. Second gradient of strain and surface-tension in linear elasticity. Int J Solids Struct. 1965;1(4):417-38. https://doi.org/10.1016/0020-7683(65)90006-5
7. Fleck NA, Hutchinson JW. A reformulation of strain gradient plasticity. J Mech Phys Solids. 2001;49(10):2245-71. https://doi.org/10.1016/S0022-5096(01)00049-7
8. Qi L, Wang Z, Sun Y, Khorami M, Mahmoudi T, Wu H. Modified couple stress and artificial intelligence examination of nonlinear buckling in porous variable thickness cylinder micro sport structures. Mech Adv Mater Struct. 2024;31(29):12135-53. https://doi.org/10.1080/15376494.2024.2316795
9. Garg A, Belarbi MO, Li L, Tounsi A. On application of machine learning techniques for predicting the bending and buckling behavior of FGM nanobeams. Adv Nano Res. 2024;17(5):445-54. https://doi.org/10.12989/anr.2024.17.5.445
10. Cheng X, Al-Khafaji SH, Hashemian M, Ahmed M, Eftekhari SA, Alanssari AI, et al. Statistical analysis and neural network modeling of functionally graded porous nanobeams vibration in an elastic medium by considering the surface effects. Eng Appl Artif Intell. 2023;123:106313. https://doi.org/10.1016/j.engappai.2023.106313
11. Tariq A, Uzun B, Deliktaş B, Yaylı MÖ. Application of machine learning methodology for investigating the vibration behavior of functionally graded porous nanobeams. J Strain Anal Eng Des. 2025;60(2):131-51. https://doi.org/10.1177/03093247241278391
12. Zheng F, Lu Y, Duan R, Chen X, Koochakianfard O. Machine learning and numerical approaches for vibration behavior prediction of rotating nanobeams in complex environments. Mech Adv Mater Struct. 2025;32(15):3706-23. https://doi.org/10.1080/15376494.2024.2395507
13. Demir E, Sayer M, Callioglu H. An approach for predicting longitudinal free vibration of axially functionally graded bar by artificial neural network. Proc Inst Mech Eng C J Mech Eng Sci. 2023;237(10):2245-55. https://doi.org/10.1177/09544062221141246
14. Mahesh V. Nonlinear frequencies of porous functionally graded piezo-elasto-magneto plates with non-uniform thickness: a hybrid FEM-ANN predictive approach. Acta Mech. 2024;235(2):633-57. https://doi.org/10.1007/s00707-023-03768-z
15. Jain R, Azam MS, Singh PP. Bending analysis of functionally graded plates resting on elastic foundation: a Rayleigh-Ritz approach and ANN method. Mech Adv Mater Struct. 2024;31(29):11484-502. https://doi.org/10.1080/15376494.2024.2307474
16. Jain R, Azam MS. Effect of partial elastic foundation on the bending behavior of functionally graded tapered porous plates utilizing Rayleigh-Ritz approach and deformation prediction with artificial neural network. Int J Interact Des Manuf. 2025;19(8):5893-915. https://doi.org/10.1007/s12008-024-02178-2
17. Wang S, Qian Z, Shang Y. Size-dependent vibration analysis of porous 3D-FG microshells in complex thermal environments using a neural network enhanced finite element model. Case Stud Therm Eng. 2024;61:104887. https://doi.org/10.1016/j.csite.2024.104887

18. Do DTT, Lee D, Lee J. Material optimization of functionally graded plates using deep neural network and modified symbiotic organisms search for eigenvalue problems. Compos B Eng. 2019;159:300-26. https://doi.org/10.1016/j.compositesb.2018.09.087
19. Lim CW, Zhang G, Reddy JN. A higher-order nonlocal elasticity and strain gradient theory and its applications in wave propagation. J Mech Phys Solids. 2015;78:298-313. https://doi.org/10.1016/j.jmps.2015.02.001
20. Barati MR. On wave propagation in nanoporous materials. Int J Eng Sci. 2017;116:1-11. https://doi.org/10.1016/j.ijengsci.2017.03.007
21. Aria AI, Rabczuk T, Friswell MI. A finite element model for the thermo-elastic analysis of functionally graded porous nanobeams. Eur J Mech A Solids. 2019;77:103767. https://doi.org/10.1016/j.euromechsol.2019.04.002
22. Li L, Tang H, Hu Y. The effect of thickness on the mechanics of nanobeams. Int J Eng Sci. 2018;123:81-91. https://doi.org/10.1016/j.ijengsci.2017.11.021
23. Tang H, Li L, Hu Y. Coupling effect of thickness and shear deformation on size-dependent bending of micro/nano-scale porous beams. Appl Math Model. 2019;66:527-47. https://doi.org/10.1016/j.apm.2018.09.027
24. Tang H, Li L, Hu Y, Meng W, Duan K. Vibration of nonlocal strain gradient beams incorporating Poisson's ratio and thickness effects. Thin-Walled Struct. 2019;137:377-91. https://doi.org/10.1016/j.tws.2019.01.027
25. Eltaher MA, Mahmoud FF, Assie AE, Meletis EI. Coupling effects of nonlocal and surface energy on vibration analysis of nanobeams. Appl Math Comput. 2013;224:760-74. https://doi.org/10.1016/j.amc.2013.09.002
26. Ghazwani MH, Alnujaie A, Avcar M, Vinh PV. Examination of the high-frequency behavior of functionally graded porous nanobeams using nonlocal simple higher-order shear deformation theory. Acta Mech. 2024;235(5):2695-714. https://doi.org/10.1007/s00707-024-03858-6
27. Saffari S, Hashemian M, Toghraie D. Dynamic stability of functionally graded nanobeam based on nonlocal Timoshenko theory considering surface effects. Physica B. 2017;520:97-105. https://doi.org/10.1016/j.physb.2017.06.029
28. Bouhadra A, Menasria A, Rachedi MA. Boundary conditions effect for buckling analysis of porous functionally graded nanobeam. Adv Nano Res. 2021;10(4):313-25. https://doi.org/10.12989/anr.2021.10.4.313
29. Eltaher MA, Fouda N, El-midany T, Sadoun AM. Modified porosity model in analysis of functionally graded porous nanobeams. J Braz Soc Mech Sci Eng. 2018;40(3):141. https://doi.org/10.1007/s40430-018-1065-0
30. Eltaher MA, Emam SA, Mahmoud FF. Free vibration analysis of functionally graded size-dependent nanobeams. Appl Math Comput. 2012;218(14):7406-20. https://doi.org/10.1016/j.amc.2011.12.090
31. Rahmani O, Pedram O. Analysis and modeling the size effect on vibration of functionally graded nanobeams based on nonlocal Timoshenko beam theory. Int J Eng Sci. 2014;77:55-70. https://doi.org/10.1016/j.ijengsci.2013.12.003